Hybrid and Inorganic Vacancy-Ordered Double Perovskites A_2WCl_6

Emily E. Morgan,[†] Greggory T. Kent,[†] Arava Zohar,[†] Anthony O'Dea,[†] Guang Wu,[‡] Anthony K. Cheetham,[*,†,¶] and Ram Seshadri[*,†,‡]

[†]Materials Department and Materials Research Laboratory

University of California, Santa Barbara, California 93106, United States

[‡]Department of Chemistry and Biochemistry

University of California, Santa Barbara, California 93106, United States

[¶]Department of Materials Science and Engineering

National University of Singapore, Singapore 117575, Singapore

E-mail: akc30@cam.ac.uk; seshadri@mrl.ucsb.edu

Abstract

We report hybrid and all-inorganic, vacancy-ordered double perovskites of d^2 W^{4+} with the formulae A_2WCl_6 (A = $CH_3NH_3^+$, Rb^+, and Cs^+). These compounds, which are reddish in color, can be distinguished from structurally similar compounds obtained by hydrothermal methods on the basis of structure, spectroscopic, and magnetic properties. The latter are green and incorporate oxygen, with actual formulae $Cs_2WO_xCl_{6-x}$ and distinct optical absorption and emission behavior. The local-moment magnetism of the pure red d^2 compounds reported here do not correspond to the appropriate Kotani model, suggesting as-yet undiscovered physics in these systems.

Introduction

The K_2PtCl_6 structure type — more familiarly referred to as the vacancy-ordered double perovskite — was first identified in 1834,[1,2] with the crystal structure established by Dickinson[3] in 1922. In recent years, compounds with this crystal structure have emerged as promising materials for optoelectronic applications. The structure type is defined by the formula A_2MX_6, where A is a monovalent cation such as Cs^+ or $CH_3NH_3^+$ (MA), M is a metal in the $4+$ oxidation state, and X is a halide anion. As implied by the name, the structure of these compounds can be visualized as a double perovskite in which the second M' site is vacant, resulting in isolated $MX_6{}^{2-}$ octahedra bound electrostatically by A-site cations.[4,5] Despite the lack of continuous cation–anion–cation connectivity, the iodide compounds display disperse bands as a consequence of the extended and polarizable orbitals on the anion.[4,6,7] Therefore, recent interest in these compounds has been driven by the potential use of Cs_2SnI_6[4] and Cs_2TeI_6[6,8] as photovoltaic materials. Additionally, computational studies have explored the electronic structures of many members of the vacancy-ordered family and revealed structure-property relationships that can be used to select compounds with the most promising optoelectronic characteristics.[9–12]

Many early transition metal oxides prefer metal–metal bonding as a means of dealing with unpaired d electrons[13] which makes magnetic compounds with d^1, d^2, *etc.* configurations elusive. In the structure type described here, transition metal ions are forced to be somewhat distant, obviating metal–metal bonding, and permitting magnetism to manifest. Consequently, vacancy-ordered double perovskites based on transition metals have been used as model systems to study magnetism. For example, compounds such as Cs_2NbX_6 and Cs_2TaX_6 have revealed the influence of the X-site on magnetic properties,[14] and Cs_2TaCl_6 shows particularly interesting low-temperature magnetism.[15,16] Recently, some of us have reported a family of compounds with the general composition A_2RuX_6[17,18] where the identity of the A-site and X-site can be used to tune the effective strength of spin-orbit coupling in these compounds, as determined by fitting magnetic data to models proposed by

Kotani.[19] Given the interesting trends revealed in these prior works, we wished to understand if similar behavior is seen in compounds with the overall formula A_2WX_6. It was also of interest to determine whether hybrid halide compounds of magnetic d^2 W^{4+} could be obtained.

There are a few reports of A_2WX_6 compounds where A = K, Rb, Cs, Ba, or Tl and X = Cl or Br. A solid-state synthesis from the alkali chloride salts and WCl_6 yielded reddish powders of A_2WCl_6.[20] Additionally, a single crystal structure study of Cs_2WCl_6 confirmed the red color and vacancy-ordered structure of this compound, but no further characterization was reported.[21] Interestingly, a more recent report has suggested that Cs_2WCl_6 and Cs_2MoCl_6 can be obtained from hydrothermal synthesis in HCl and describes both as forming green crystals displaying bright near-IR emission.[22]

Given that the reported properties of Cs_2WCl_6 appear to vary significantly depending on the synthesis method, we sought to synthesize the A_2WX_6 compounds and determine their compositions, structures, and properties. We find that they can be most easily prepared by combining the appropriate A-cation salt and WCl_4 under anaerobic and anhydrous conditions. This set of compounds shows trends in their optical properties that are similar to what was observed in other vacancy-ordered systems.[18] Additionally, we have found that magnetism in these compounds deviates from the Kotani model; however, the reasons for this behavior remain unclear. Finally, we demonstrate that these A_2WX_6 compounds, which do not show strong optical emission, are compositionally distinct from the compounds produced by hydrothermal synthesis, which do. This difference in composition is central to explaining the different observed optical properties.

Experimental Methods

Synthesis

All reagents were purchased from Fisher Scientific or Sigma Aldrich. With the exception of solvents, all other materials were used without further purification or modification. In the case of solvents, diethyl ether (Et_2O) and acetonitrile (MeCN) were dried using a Vacuum Atmospheres DRI-SOLV Solvent Purification system and stored over $3\,\text{Å}$ molecular sieves prior to use. All handling of air-sensitive reagents and products was performed under anaerobic and anhydrous conditions in a nitrogen-filled glovebox.

A_2WCl_6 compounds were synthesized by combining $0.25\,\text{mmol}$ of the appropriate A-cation salt (CsCl, RbCl, or CH_3NH_3Cl (MACl)) and $0.125\,\text{mmol}$ of WCl_4 in $5\,\text{mL}$ of acetonitrile and stirring. In the case of MA_2WCl_6, the solution changes color to a dark reddish-purple after a few hours, and the reaction is complete after stirring for 24 hours. The majority of the product forms as a microcrystalline powder; however, single crystals can be collected from the solid deposited on the sides of the vial during stirring. The powder can be washed with diethyl ether and isolated by filtration. In the case of Cs_2WCl_6 and Rb_2WCl_6, the reaction is complete after stirring for 5 days (due to the low solubility of the salts in acetonitrile). Cs_2WCl_6 is a dark orange and Rb_2WCl_6 is reddish-purple. The products form as very fine powders and no single crystals could be obtained. The powders were isolated by washing with diethyl ether and carefully decanting away the liquid phase to isolate the solid.

For the sake of comparison with the literature, we also attempted to synthesize Cs_2WCl_6 from a solvothermal synthesis in acid. In this case, the synthesis followed a modified version of the literature report.[22] $0.25\,\text{mmol}$ of CsCl was combined with $0.125\,\text{mmol}$ of WCl_4 and $3\,\text{mL}$ of concentrated hydrochloric acid in a hydrothermal vessel. The vessel was heated to $160\,°C$ for 2 days, followed by slow cooling to room temperature for 24 hours, producing bright green crystals. Single crystal X-ray diffraction reveals that the

composition of these crystals is $Cs_2WO_{1.08}Cl_{4.92}$.

Single-crystal X-ray diffraction

Single-crystal X-ray diffraction data was collected on a KAPPA APEX II diffractometer with an APEX II CCD detector, TRIUMPH monochromator, and Mo-Kα radiation source (λ = 0.71073 Å). For moisture-sensitive samples, nitrogen was blown over the sample during data collection using an Oxford nitrogen gas cryostream system. Data collection was performed at 298 K for MA_2WCl_6 and 100 K for $Cs_2WO_{1.08}Cl_{4.92}$. Data collection and cell parameter determination were conducted using the SMART program. Integration of the data frames and final cell parameter refinement were performed using SAINT software. Absorption corrections of the data were carried out using the multi-scan method SADABS. Structure solution and refinement were performed using SHELXTL. All crystal structures are visualized using the VESTA software package.[23] Further crystallographic details can be found in the Supporting Information.

Synchrotron X-ray diffraction

High-resolution synchrotron powder X-ray diffraction data were collected at beamline 11-BM at the Advanced Photon Source at Argonne National Laboratory. The powder X-ray diffraction data were analyzed using the TOPAS software suite.[24] Initial Pawley refinements[25] were performed to determine lattice parameters and peak shapes. Subsequently, Rietveld refinements were performed to determine background, zero-point error, atomic positions, and isotropic ADPs. In the case of Cs_2WCl_6, the sample contained some residual CsCl from the reaction mixture, so CsCl was included as a second phase in the refinement.

X-ray photoelectron spectroscopy

X-ray photoelectron spectroscopy measurements were performed using a Thermo Fisher Escalab Xi+ XPS system with a monochromated aluminum anode (1486.7 eV). Powder samples were pressed onto carbon tape and were transferred to the instrument using a homemade air-free sample holder. Since all measured samples were semiconducting, charge compensation was applied and all spectra were referenced to the C $1s$ peak of carbon at 284.5 eV. Data fitting was performed using the CasaXPS software package. For fitting of the tungsten high-resolution spectra, several constraints were imposed. The $4f$ 5/2 peak was required to have 3/4 of the area of the 7/2 peak and the same FWHM. Additionally, the two pairs of 5/2 and 7/2 peaks were required to have the same separation in binding energy.

Raman spectroscopy and photoluminescence measurements

Raman spectroscopy and photoluminescence measurements were performed at room temperature using a Horiba Jobin Yvon T64000 open-frame confocal microscope operating at a wavelength of 488 nm with triple monochromator and LN2-cooled CCD array detector. Filters were used to reduce the laser to 25% of its original intensity to prevent beam damage to the samples. For air-sensitive samples, the powders were loaded into a homemade air-free cell with a fused silica window (Corning glass) inside a glovebox. Spectra were calibrated by referencing the spectrum of monocrystalline silicon, which has a peak at $521 \, cm^{-1}$. Additionally, the spectrum of silicon inside the air-free cell was used to confirm that the use of the cell only contributes very minor peaks or changes to the baseline, as shown in the Supporting Information.

UV-vis spectroscopy

Absorbance spectra were obtained by measuring diffuse reflectance on a Shimadzu UV3600 UV-Vis-NIR spectrometer equipped with an integrating sphere. Samples were diluted in barium sulfate. Air-sensitive samples were transferred to the sample holder inside of the glovebox and a glass coverslip was attached to the front of the sample holder to minimize air exposure. Reflectance was converted to absorbance using the Kubelka-Munk transformation.[26]

Magnetic measurements and data processing

Magnetic measurements were performed on a Quantum Design MPMS3 Squid instrument. DC measurements were performed in VSM mode. Approximately $10\,mg$ of sample was deposited inside plastic capsules purchased from Quantum Design, which was mounted in a brass sample rod. Magnetization vs temperature measurements were performed at fields of $500\,Oe$ and $7\,T$ between $1.8\,K$ and $300\,K$. To calculate the temperature-dependent effective moment for each sample, the magnetization was converted to susceptibility (χ). For the Kotani fitting, a diamagnetic correction factor equal to $(molar\,mass/2) \times 10^{-6}$ was added to the susceptibility values. The effective moment at each temperature was calculated as $2.827\sqrt{\chi T}$. For the Kotani fitting, Equations 1 and 2 for the effective moments were used for the d^1 and d^2 cases, respectively. In these equations, $x = \frac{A}{kT}$ where A represents the strength of spin-orbit coupling in cm^{-1}, k is the Boltzmann constant, and T is the temperature. For the Curie-Weiss fitting, the $1/\chi$ data was fit using Equation 3, where χ_0 is the diamagnetic correction to the susceptibility, T is the temperature, C is the Curie constant, and θ_{CW} is the Weiss temperature.

$$n_{eff}^2 = \frac{8 + (3x - 8)e^{\frac{-3}{2}x}}{x(2 + e^{\frac{-3}{2}x})} \tag{1}$$

$$n^2_{eff} = \frac{3\{\frac{5}{2}x + 15 + (\frac{x}{2} + 9)e^{-x} - 24e^{\frac{-3}{2}x}\}}{x(5 + 3e^{-x} + e^{\frac{-3}{2}x})} \tag{2}$$

$$\chi^{-1} = \frac{T - \theta_{CW}}{\chi_0(T - \theta_{CW}) + C} \tag{3}$$

Results and Discussion

The compounds MA_2WCl_6, Rb_2WCl_6, and Cs_2WCl_6 were prepared by combining a stoichiometric ratio of the *A*-cation chloride salt and WCl_4 in anhydrous acetonitrile and stirring for several days at room temperature, as described in the Experimental Methods. Due to the air- and moisture-sensitivity of these compounds, they were prepared and stored in a nitrogen-filled glovebox. In the case of MA_2WCl_6, maroon single crystals could be obtained directly from the reaction mixture. For Rb_2WCl_6 and Cs_2WCl_6, the compounds were insoluble in organic solvents and precipitated as fine reddish-orange and purple powders, respectively.

The crystal structures of MA_2WCl_6 and Cs_2WCl_6 as determined from single-crystal X-ray diffraction (XRD) and synchrotron XRD, respectively, are shown in Figure 1. The compound MA_2WCl_6 crystallizes in the trigonal space group $R\bar{3}m$. Notably, we believe this to be the first true hybrid vacancy-ordered halide perovskite structure based on tungsten. This compound is structurally analogous to MA_2RuCl_6,[17] and similarly to this compound, the octahedra are very regular, despite not being constrained by symmetry. The unique bond angles are 90.44° and 89.56° and W–Cl bond distances are all 2.3782(18) Å. The structure type is stabilized by hydrogen bonding, with a minimum N···Cl distance of 3.447(8) Å. The alignment of the methylammonium cations in this structure maximizes their hydrogen bonding interactions of the NH_3^+ group with the Cl^- anions. Due to the larger size of tungsten, its unit cell is slightly larger than that of the ruthenium analogue, with $a = 7.1125(14)$ Å and $c = 21.975(6)$ Å. Synchrotron X-ray diffraction data, showing that the
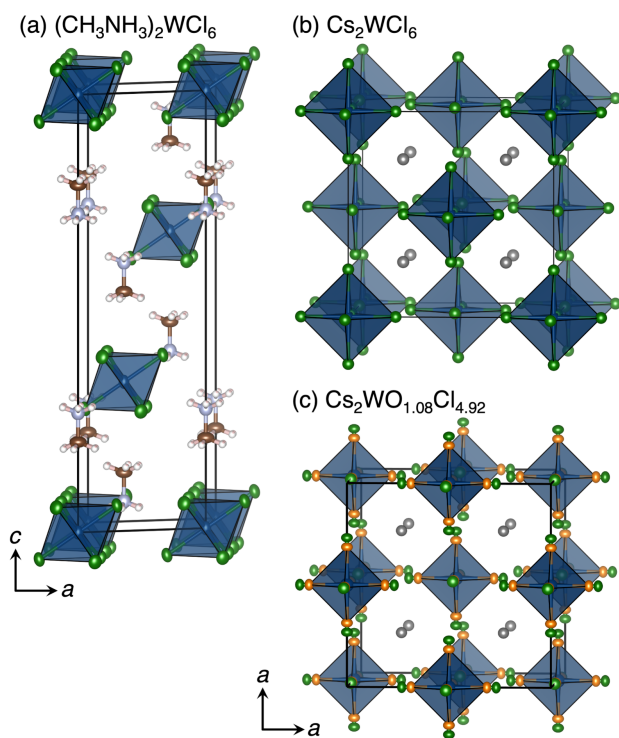
Figure 1: (a) Single crystal structure of MA_2WCl_6 with thermal displacement ellipsoids depicted at 50 % probability. (b) Structure of Cs_2WCl_6 as determined from synchrotron XRD. (c) Single crystal structure of $Cs_2WO_{1.08}Cl_{4.92}$ with thermal displacement ellipsoids depicted at 50 %.

single-crystal structure is consistent with the structure of the bulk powder, is shown in the Supporting Information.
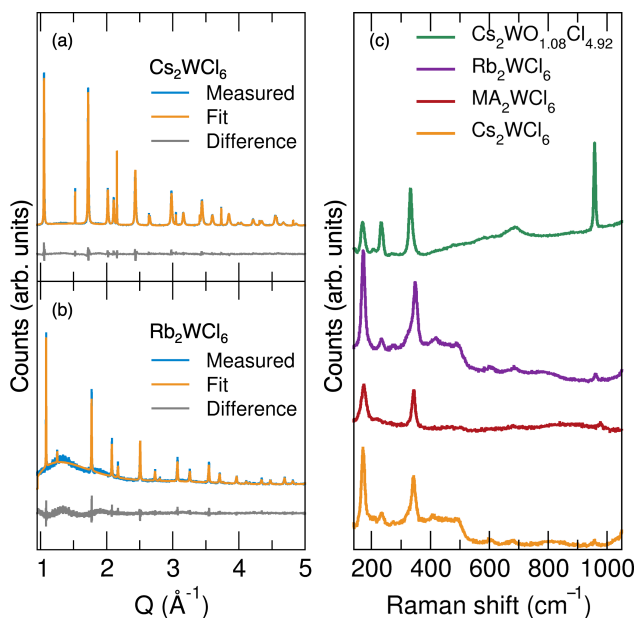

Figure 2: 11-BM synchrotron X-ray diffraction data, fit, and difference for (a) Cs_2WCl_6, $R_{wp} = 7.27\%$, $R_p = 5.97\%$. The refinement includes CsCl as a secondary phase. (b) Rb_2WCl_6 $R_{wp} = 8.92\%$, $R_p = 7.26\%$. The broad hump in the diffraction pattern between $Q = 1.0\,\text{Å}^{-1}$ and $2.0\,\text{Å}^{-1}$ is due to the kapton sample holder. (c) Raman spectra for A_2WCl_6 compounds and $Cs_2WO_{1.08}Cl_{4.92}$.

The compounds Rb_2WCl_6 and Cs_2WCl_6 were difficult to recrystallize due to low solubility in organic solvents, so the structures were determined by synchrotron X-ray diffraction of the powders, shown in Figure 2(a) and (b). For these compounds, which both crystallize in the space group $Fm\bar{3}m$, we found that their structures are similar, but not identical, to what has been reported in the literature.[21] Pawley and Rietveld refinements indicate that Rb_2WCl_6 has a cubic cell parameter of 10.02(1) Å, and Cs_2WCl_6 has a cell parameter of 10.326(2) Å. The lattice parameter for Cs_2WCl_6 is larger than the previously-reported value of 10.245(1) Å determined from single crystal diffraction,[21] and the value of 10.27 Å estimated from powder Debye X-ray photographs.[20] One potential explanation for this discrepancy is simply the different diffraction techniques used in the structure determinations. A second possibility is that the differences in cell parameters could reflect differences in

composition due to the use of different synthetic strategies.

To further explore the relationship between the synthesis method and the properties of the A_2WCl_6 compounds, we attempted to synthesize Cs_2WCl_6 using a hydrothermal method reported in the literature.[22] This synthesis produces bright green cuboctahedral crystals, and a single-crystal XRD refinement for these crystals gives a cell parameter of 10.23(2) Å. Furthermore, this compound is stable under ambient conditions, which contrasts with the air- and moisture-sensitivity of the other synthesized A_2WX_6 compounds. Suspecting that there must be a difference in composition between the hydrothermal product and the compounds prepared under inert conditions, we performed Raman spectroscopy, the results of which are shown in Figure 2(c). In the case of the hydrothermal compound, we observe strong peaks at $171\,cm^{-1}$, $235\,cm^{-1}$, $334\,cm^{-1}$, and $960\,cm^{-1}$. These are similar to the values reported previously for this hydrothermal product.[22] Considering the spectrum of the Cs_2WCl_6 prepared under dry and anaerobic conditions, we can see similar features at lower wavenumbers, with strong peaks at $169\,cm^{-1}$, $235\,cm^{-1}$, and $345\,cm^{-1}$, and only a very small peak at $960\,cm^{-1}$. Similarly, for Rb_2WCl_6, there are strong peaks at $173\,cm^{-1}$, $236\,cm^{-1}$, and $348\,cm^{-1}$, and a weak peak at $960\,cm^{-1}$. MA_2WCl_6 has strong peaks at $174\,cm^{-1}$ and $344\,cm^{-1}$ and a small peak at $975\,cm^{-1}$. Based on symmetry considerations, the $Fm\bar{3}m$ structure should have only three Raman-active modes and the $R\bar{3}m$ structure should have two modes.[27–29] Furthermore, previous literature on tungsten compounds suggests that the peak at $960\,cm^{-1}$ should be attributed to the W=O bond in a $WOCl_5{}^{2-}$ distorted octahedron, while the three intense lower energy peaks are due to the motions of the W–Cl bonds.[30] Overall, the Raman spectra suggest that the hydrothermal sample contains a large number of W=O bonds, while the samples prepared under inert conditions contain very few.

Based upon our analysis of the Raman spectra, we developed a new structural model of the hydrothermal compound, which is shown in Figure 1(c). In this model, an oxygen position was added to the structure in between the W and Cl positions such that the W–O

bond distance is 1.90(8) Å and the W–Cl bond distance is 2.369(7) Å. The occupancies of the O and Cl positions were then refined and constrained to add up to one, based on the assumption that each W atom should have six-fold coordination. Using this model, we have determined the composition of the hydrothermal product to be $Cs_2WO_{1.08}Cl_{4.92}$. We believe this to be a reliable estimate, as the estimated standard deviation on the oxygen content in the formula unit is 0.07 (i.e. 1.08(7)). This suggests that the majority of octahedra in the structure will have a composition of $[WOCl_5]^{2-}$, but that there may also be some with a composition of $[WO_2Cl_4]^{2-}$. The presence of oxygen in this compound also explains observations that the hydrothermal product tends to have a smaller cell parameters, due to the higher oxidation state of W in the oxyhalide octahedra and the short W–O bonds. We also note that a similar compound was previously reported with a composition of Cs_2WOCl_5;[30] however, a full single-crystal structure solution has not been obtained until now. After examining a number of samples prepared using this hydrothermal method, we have found that the oxygen content, as determined by this type of refinement, can vary between 1 and 1.5 oxygen per formula unit. In addition to the Raman data and cell parameter trends, a clear justification for the use of our model is that if the structure is refined with the incorrect composition of Cs_2WCl_6 the R-factor is 3.53%, while the R-factor for $Cs_2WO_{1.08}Cl_{4.92}$ is 2.54%. This result is consistent with previous findings that a $M=O$ bond can closely resemble a $M-Cl$ bond in single crystal diffraction and refinements of disordered compounds,[31] and in this case leads to a large reduction in R-factor.

Given the fact that Cs_2WCl_6 and $Cs_2WO_{1.08}Cl_{4.92}$ appear similar in diffraction data, it was important to further evaluate the composition of these samples. High-resolution XPS spectra, shown in Figure 3(a) and (b), were examined to determine the oxidation state of W in each sample. Additionally, we compared the XPS survey scans for Cs_2WCl_6 and $Cs_2WO_{1.08}Cl_{4.92}$ (shown in the Supporting Information) to verify that Cs_2WCl_6 contains a higher proportion of Cl, while $Cs_2WO_{1.08}Cl_{4.92}$ contains more O. All of the W XPS spectra examined showed similar features, with two sets of doublets corresponding to the
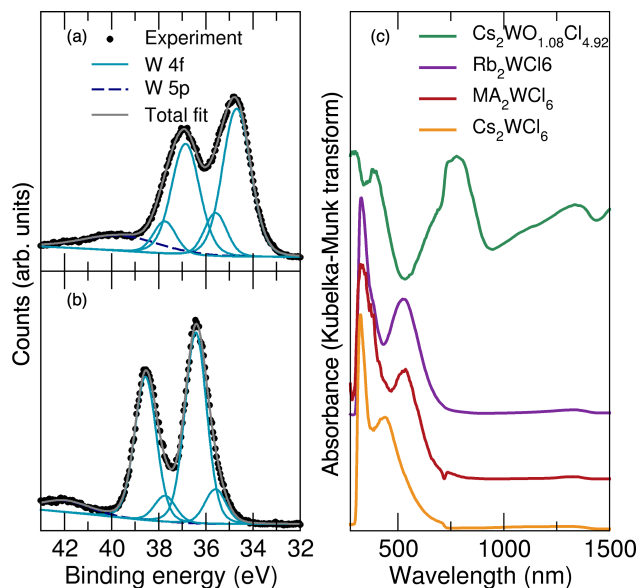
Figure 3: XPS spectra for the W 4f and 5p regions of (a) Cs_2WCl_6 and (b) $Cs_2WO_{1.08}Cl_{4.92}$. (c) Kubelka-Munk transformed UV-vis spectra for A_2WCl_6 compounds and $Cs_2WO_{1.08}Cl_{4.92}$.

$4f$ photoelectron peaks, and one peak at higher binding energy corresponding to the $5p$ photoelectron peak. For Cs_2WCl_6, the most intense $4f_{\frac{7}{2}}$ and $4f_{\frac{5}{2}}$ photoelectron peaks, which we attribute to W^{4+}, occur at 34.7 eV and 36.9 eV. These values are similar to those for Rb_2WCl_6 (34.7 eV and 36.9 eV) and MA_2WCl_6 (34.6 eV and 36.8 eV). The W high-resolution spectra for these compounds are displayed in the Supporting Information. In the case of $Cs_2WO_{1.08}Cl_{4.92}$, the most intense $4f$ peaks, which we attribute to W^{5+}, occur at 36.4 eV and 38.6 eV. For all the samples, an additional set of W $4f$ photoelectron peaks is present, in which the $4f_{\frac{7}{2}}$ peak is observed at 35.6 eV and the $4f_{\frac{5}{2}}$ at 37.7 eV. Given that these peaks are observed with similar intensities and locations in all compounds, we attribute them to the presence of surface oxidation in the samples. This oxidation may also provide an explanation for the weak peaks at $960\,\mathrm{cm}^{-1}$ observed in the Raman spectra of the A_2WX_6 compounds.

The UV-vis absorbance data for the A_2WCl_6 compounds is shown in Figure 3(c). As expected from the appearance of the two compounds, the absorbance profiles of MA_2WCl_6 and Rb_2WCl_6 are very similar, with both showing absorbance maxima at 530 nm and

14

327 nm. Similarly to the analogous ruthenium compounds[18] and previous literature reports,[20] the absorption maxima for Cs_2WCl_6 are shifted to higher energy, and occur at 440 nm and 323 nm. This is because the larger Cs^+ cations decrease the interactions between the $[WCl_6]^{2-}$ octahedra, leading to a less-disperse valence band and higher-energy absorption onset for this compound. The lower-energy maxima in all the A_2WCl_6 compounds are attributed to $d-d$ transitions, while the higher-energy features are ligand-to-metal charge transfer (LMCT) transitions.[20] The spectra for the A_2WCl_6 compounds are clearly different from the spectrum of $Cs_2WO_{1.08}Cl_{4.92}$, which shows two broad peaks with maxima at approximately 400 nm and 800 nm. Using the molecular-orbital diagram developed by Gray $et.$ $al.$ for the molybdenyl ion,[32,33] we can assign these features to the d_{xy} to $d_{x^2-y^2}$ and d_{xy} to d_{xz}, d_{yz} transitions, respectively. A simplified version of this molecular-orbital diagram is reproduced in the Supporting Information. Here, the $[WOCl_5]^{2-}$ unit is non-centrosymmetric, therefore enhancing the intensity of the $d-d$ transitions compared to those in A_2WCl_6. Additionally, some higher-energy absorption features are visible for wavelengths shorter than 400 nm. These likely correspond to the d_{xy} to d_{z^2} and LMCT transitions.

We also confirmed that $Cs_2WO_{1.08}Cl_{4.92}$ displays intense photoemission with a maximum around 900 nm under 488 nm laser excitation (spectrum shown in the Supporting Information). In contrast, the A_2WCl_6 compounds do not emit under these conditions. Based on the difference in the optical properties, it is clear that the substitution of O for Cl plays a key role in near-IR emission. Again using the molecular-orbital diagram[32,33] we suggest that the emission arises from a $d-d$ transition. This explanation for the optical properties differs from that in previous work, which attributes the luminescence to self-trapped excitons which induce a large Stokes shift.[22]

Earlier works on the A_2WCl_6 compounds indicate that their magnetic behavior is not consistent with the Kotani model, and suggest that this deviation originates from antiferromagnetic interactions.[20] Therefore, it was of interest to determine whether our compounds
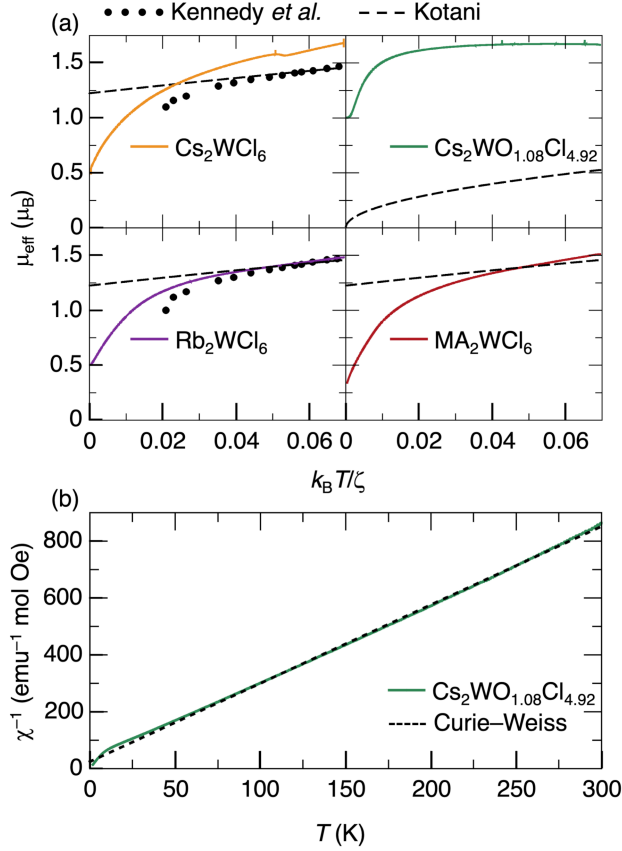
Figure 4: (a) Temperature dependence of the effective moment of the A_2WCl_6 compounds and $Cs_2WO_{1.08}Cl_{4.92}$, as well as comparison with previous reports and theory. The spin-orbit coupling parameter ζ is assumed to be $3000\,\mathrm{cm}^{-1}$. (b) Curie-Weiss fit of the magnetic data for $Cs_2WO_{1.08}Cl_{4.92}$. The Weiss temperature is $-8.92\,\mathrm{K}$ and the effective moment is $1.70\,\mu_B$.

displayed this same behavior. Figure 4 demonstrates that our measurements on Cs_2WCl_6 and Rb_2WCl_6 are similar to this previously-reported data. Additionally, none of the data can be adequately fit to the Kotani model for d^2 ions.[19] This model is used to account for the influence of the orbital angular momentum on the temperature-dependence of the effective magnetic moment for transition metal ions in an octahedral field. By fitting magnetic data to the appropriate Kotani equation, the strength of spin-orbit coupling in a compound can be determined. Here, we have assumed a spin-orbit coupling constant of $3000\,cm^{-1}$, which is similar to the constant that is predicted for a free W^{4+} ion.[34] However, for any value chosen for the spin-orbit coupling, it is not possible to fit the data, because at low temperatures the observed moment is significantly lower than theoretically predicted. Regardless of spin-orbit coupling constant, all Kotani d^2 ions should converge to a moment of $1.22\,\mu_B$ at $0\,K$,[19] while our A_2WCl_6 compounds all show low-temperature moments of approximately $0.5\,\mu_B$. Therefore, it is reasonable to attribute the discrepancy to antiferromagnetic interactions. However, the closest W–W distance in these structures is $7.088\,\text{Å}$ in Rb_2WCl_6, so we do not believe that there could be direct antiferromagnetic exchange between the W atoms. Additionally, we emphasize that the discrepancy between theory and experiment does not appear to be due to the onset of an antiferromagnetic transition, as the curvature of the lines describing the effective moments for theory and experiment are different even at intermediate temperatures. Works on related compounds have hypothesized that antiferromagnetic interactions could be mediated by the delocalization of unpaired electrons onto the chloride ligands;[35] however, further study is required to determine the precise mechanism of this interaction and whether this is the case in these compounds.

For comparison, we also show the magnetic behavior of the $Cs_2WO_{1.08}Cl_{4.92}$ compound and plot it with the Kotani model for a d^1 metal. In this case the discrepancy between theory and experiment is expected, because the $WOCl_5{}^{2-}$ ion does not have ideal octahedral symmetry. The lowering of symmetry quenches the orbital angular momentum,

17

which should lead to an effective moment that is close to the spin-only value for a single unpaired electron.[35,36] A Curie-Weiss fit of the magnetic data for this compound, shown in Figure 4(b), gives a Weiss temperature of $-8.92\,\mathrm{K}$, a Curie constant of $0.362\,\mu_B^2$, and an effective moment of $1.70\,\mu_B$. As expected, this is close to the theoretical moment for a single unpaired electron, which is $1.73\,\mu_B$.

Conclusion

In summary, the vacancy-ordered double perovskites $A_2\mathrm{WCl}_6$ (A = MA (CH$_3$NH$_3$$^+$), Rb, and Cs) and the oxyhalide $\mathrm{Cs_2WO_{1.08}Cl_{4.92}}$ have been studied. MA$_2$WCl$_6$ constitutes the first report of a hybrid W halide with a perovskite-related structure. We have also shown that $\mathrm{Cs_2WCl_6}$ and $\mathrm{Cs_2WO_{1.08}Cl_{4.92}}$ closely resemble one another in diffraction data, but can be distinguished *via* spectroscopy, magnetism, and even by eye. For example, the appearance of an intense peak in the Raman spectrum around $960\,\mathrm{cm^{-1}}$ is a clear sign of W=O bonds. $\mathrm{Cs_2WO_{1.08}Cl_{4.92}}$ has two broad absorption maxima in the visible range and shows intense photoluminescence in the near-IR regime under 488 nm laser excitation. The incorporation of O into this compound is significant to its optical properties, and we believe that it is the splitting of the d orbitals, due to the lower symmetry of the WOCl$_5$$^{2-}$ ion, that gives rise to the distinct absorption features and bright emission. Interestingly, the structure and optical properties of similar compounds have previously been studied,[36,37] and Cs$_2$NbOF$_5$ has also been identified as a strong emitter with a large Stokes shift, attributed to a self-trapped state.[38] Therefore, it may be worthwhile to re-examine the optical properties of these related compounds in future works. Additionally, we note that the results reported here for the differences between the compounds $\mathrm{Cs_2WCl_6}$ and $\mathrm{Cs_2WO_{1.08}Cl_{4.92}}$ should also apply to the molybdenum-based versions. We have also attempted to synthesize the pure $A_2\mathrm{MoCl}_6$ compounds using a number of methods; however, we find that the oxychlorides will always be preferentially formed. Therefore, we believe that the materials

reported as Cs_2MoCl_6 by Liu *et. al* are probably $Cs_2MoO_xCl_{6-x}$ Finally, the magnetic behavior of Rb_2WCl_6 and Cs_2WCl_6 are similar to those reported by Kennedy *et. al.*,[20] but the temperature-dependence of the effective magnetic moment cannot be explained using the Kotani model and remains an open challenge which we plan to explore in future works.

Supporting Information

Additional crystallographic information for single-crystal and synchrotron XRD refinements (Tables S1-S6, Figure S1), near-IR luminescence of $Cs_2WO_{1.08}Cl_{4.92}$ (Figure S2), MO diagram for the $[WOCl_5]^{2-}$ ion (Figure S3), Raman spectrum of Si used for calibration and background determination (Figure S4), and additional XPS spectra (Figures S5-S7).

Acknowledgements

References

(1) Berzelius, J. J. Untersuchung über die Eigenschaften des Tellurs. *Ann. Phys. Chem* **1834**, *108*, 577.

(2) Wolf, N. R.; Connor, B. A.; Slavney, A. H.; Karunadasa, H. I. Doubling the Stakes: The Promise of Halide Double Perovskites. *Angew. Chem. Int. Ed.* **2021**, *60*, 16264–16278.

(3) Dickinson, R. G. The Crystal Structures of Potassium Chloroplatinite and of Potassium and Ammonium Chloropalladites. *J. Am. Chem. Soc.* **1922**, *44*, 2404–2411.

(4) Lee, B.; Stoumpos, C. C.; Zhou, N.; Hao, F.; Malliakas, C.; Yeh, C.-Y.; Marks, T. J.; Kanatzidis, M. G.; Chang, R. P. H. Air-Stable Molecular Semiconducting Iodosalts for Solar Cell Applications: Cs_2SnI_6 as a Hole Conductor. *J. Am. Chem. Soc.* **2014**, *136*, 15379–15385.

(5) Maughan, A. E.; Ganose, A. M.; Scanlon, D. O.; Neilson, J. R. Perspectives and Design Principles of Vacancy-Ordered Double Perovskite Halide Semiconductors. *Chem. Mater.* **2019**, *31*, 1184–1195.

(6) Maughan, A. E.; Ganose, A. M.; Bordelon, M. M.; Miller, E. M.; Scanlon, D. O.; Neilson, J. R. Defect Tolerance to Intolerance in the Vacancy-Ordered Double Perovskite Semiconductors Cs_2SnI_6 and Cs_2TeI_6. *J. Am. Chem. Soc.* **2016**, *138*, 8453–8464.

(7) Evans, H. A.; Fabini, D. H.; Andrews, J. L.; Koerner, M.; Preefer, M. B.; Wu, G.; Wudl, F.; Cheetham, A. K.; Seshadri, R. Hydrogen Bonding Controls the Structural Evolution in Perovskite-Related Hybrid Platinum(IV) Iodides. *Inorg. Chem.* **2018**, *57*, 10375–10382.

(8) Vázquez-Fernández, I.; Mariotti, S.; Hutter, O. S.; Birkett, M.; Veal, T. D.; Hobson, T. D. C.; Phillips, L. J.; Danos, L.; Nayak, P. K.; Snaith, H. J.; Xie, W.; Sherburne, M. P.;
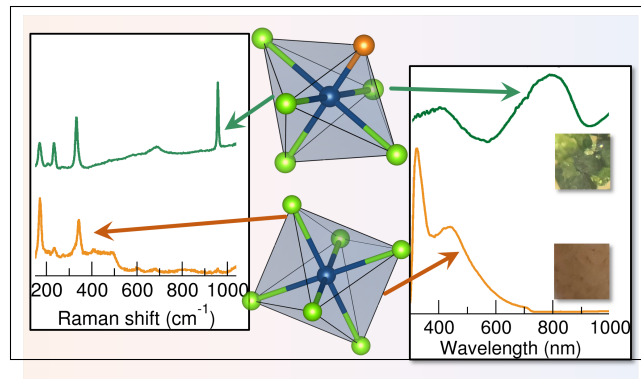
Asta, M.; Durose, K. Vacancy-Ordered Double Perovskite Cs_2TeI_6 Thin Films for Optoelectronics. *Chem. Mater.* **2020**, *32*, 6676–6684.

(9) Cai, Y.; Xie, W.; Ding, H.; Chen, Y.; Thirumal, K.; Wong, L. H.; Mathews, N.; Mhaisalkar, S. G.; Sherburne, M.; Asta, M. Computational Study of Halide Perovskite-Derived A_2BX_6 Inorganic Compounds: Chemical Trends in Electronic Structure and Structural Stability. *Chem. Mater.* **2017**, *29*, 7740–7749.

(10) Wang, Z.-Y.; Chen, Y.; Zhang, C.; Wang, D.; Liang, P.; Zhang, H.; Xie, R.-J.; Wang, L. Electronic Structure and Optical Properties of Vacancy-Ordered Double Perovskites $Cs_2PdBr_xCl_{6-x}$ by First-Principles Calculation. *J. Phys. Chem. C* **2020**, *124*, 13310–13315.

(11) Faizan, M.; Khan, S. H.; Murtaza, G.; Khan, A.; Laref, A. Electronic and Magnetic Properties of Alkali Metal Chlorides A_2MCl_6 (A = K, Rb, Cs; M = Mn, Mo): A Density Functional Theory Study. *Int. J. Mod. Phys. B* **2019**, *33*, 1950072.

(12) Faizan, M.; Bhamu, K. C.; Murtaza, G.; He, X.; Kulhari, N.; AL-Anazy, M. M.; Khan, S. H. Electronic and Optical Properties of Vacancy Ordered Double Perovskites A_2BX_6 (A = Rb, Cs; B = Sn, Pd, Pt; and X = Cl, Br, I): a First Principles Study. *Sci. Rep.* **2021**, *11*, 6965.

(13) Burdett, J. K.; Hughbanks, T. Aspects of Metal-Metal Bonding in Early-Transition-Metal Dioxides. *Inorg. Chem.* **1985**, *24*, 1741–1750.

(14) Ishikawa, H.; Yajima, T.; Matsuo, A.; Kindo, K. Ligand Dependent Magnetism of the J_{eff} = 3/2 Mott Insulator Cs_2MX_6 (M = Ta, Nb, X = Br, Cl). *J. Phys.: Condens. Matter* **2021**, *33*, 125802.

(15) Ishikawa, H.; Takayama, T.; Kremer, R. K.; Nuss, J.; Dinnebier, R.; Kitagawa, K.; Ishii, K.; Takagi, H. Ordering of hidden multipoles in spin-orbit entangled $5d^1$ Ta chlorides. *Phys. Rev. B* **2019**, *100*, 045142.

(16) Mansouri Tehrani, A.; Soh, J.-R.; Pásztorová, J.; Merkel, M. E.; Živković, I.; Rønnow, H. M.; Spaldin, N. A. Charge Multipole Correlations and Order in Cs_2TaCl_6. *Phys. Rev. Res.* **2023**, *5*, L012010.

(17) Vishnoi, P.; Zuo, J.; Strom, T. A.; Wu, G.; Wilson, S. D.; Seshadri, R.; Cheetham, A. K. Structural Diversity and Magnetic Properties of Hybrid Ruthenium Halide Perovksites and Related Compounds. *Angew. Chem.* **2020**, *59*, 8974–8981.

(18) Vishnoi, P.; Zuo, J. L.; Cooley, J. A.; Kautzsch, L.; Gómez-Torres, A.; Murillo, J.; Fortier, S.; Wilson, S. D.; Seshadri, R.; Cheetham, A. K. Chemical Control of Spin-Orbit Coupling and Charge Transfer in Vacancy-Ordered Ruthenium(IV) Halide Perovskites. *Angew. Chem.* **2021**, *133*, 5244–5248.

(19) Kotani, M. On the Magnetic Moment of Complex Ions. (I). *J. Phys. Soc. Jpn.* **1949**, *4*, 293–297.

(20) Kennedy, C.; Peacock, R. Complex Chlorides and Bromides of Quadrivalent Tungsten. *J. Chem. Soc.* **1963**, 3392–3397.

(21) Wang, P.; Xu, W.; Zheng, Y.-Q. Crystal Structure of Dicaesium Hexachloro-tungstate(IV), $Cs_2[WCl_6]$. *Z. Kristallogr. NCS* **2003**, *218*, 25–25.

(22) Liu, Z.; Qin, X.; Chen, Q.; Chen, Q.; Jing, Y.; Zhou, Z.; Zhao, Y. S.; Chen, J.; Liu, X. Highly Stable Lead-Free Perovskite Single Crystals with NIR Emission Beyond 1100 nm. *Adv. Opt. Mater.* **2022**, 2201254.

(23) Momma, K.; Izumi, F. VESTA 3 for Three-Dimensional Visualization of Crystal, Volumetric and Morphology Data. *J. Appl. Crystallogr.* **2011**, *44*, 1272–1276.

(24) Coelho, A. A. TOPAS and TOPAS-Academic: An Optimization Program Integrating Computer Algebra and Crystallographic Objects Written in C++. *J. Appl. Crystallogr.* **2018**, *51*, 210–218.

(25) Pawley, G. S. Unit-Cell Refinement from Powder Diffraction Scans. *J. Appl. Cryst.* **1981**, *14*, 357–361.

(26) Kubelka, P. Ein Beitrag zur Optik der Farbanstriche. *Z. Phys.* **1931**, *12*, 593–601.

(27) Aroyo, M. I.; Perez-Mato, J. M.; Capillas, C.; Kroumova, E.; Ivantchev, S.; Madariaga, G.; Kirov, A.; Wondratschek, H. Bilbao Crystallographic Server: I. Databases and crystallographic computing programs. *Z. Kristallogr.* **2006**, *221*, 15–27.

(28) Aroyo, M. I.; Kirov, A.; Capillas, C.; Perez-Mato, J. M.; Wondratschek, H. Bilbao Crystallographic Server. II. Representations of Crystallographic Point Groups and Space Groups. *Acta. Cryst. A* **2006**, *62*, 115–128.

(29) Kroumova, E.; Aroyo, M. I.; Perez-Mato, J. M.; Kirov, A.; Capillas, C.; Ivantchev, S.; Wondratschek, H. Bilbao Crystallographic Server: Useful Databases and Tools for Phase-Transition Studies. *Phase Trans.* **2003**, *76*, 155–170.

(30) Fergusson, J. E.; Greenaway, A. M.; Penfold, B. R. Preparative and structural studies of pentahalogeno-oxometallate(V) salts of the transition metals Cr, Mo, W, Tc, Re. *Inorg. Chim. Acta* **1983**, *71*, 29–34.

(31) Parkin, G. Bond-Stretch Isomerism in Transition Metal Complexes: a Reevaluation of Crystallographic Data. *Chem. Rev.* **1993**, *93*, 887–911.

(32) Gray, H. B.; Hare, C. R. The Electronic Structures and Spectra of Chromyl and Molybdenyl Ions. *Inorg. Chem.* **1962**, *1*, 363–368.

(33) Hare, C. R.; Bernal, I.; Gray, H. B. The Electronic Structures and Magnetic Properties of the Chromyl and Molybdenyl Ions. *Inorg. Chem.* **1962**, *1*, 831–835.

(34) Bendix, J.; Brorson, M.; Schaffer, C. E. Accurate Empirical Spin-Orbit Coupling Parameters ζ_{nd} for Gaseous nd^q Transition Metal Ions. The Parametrical Multiplet Term Model. *Inorg. Chem.* **1993**, *32*, 2838–2849.

(35) Greenaway, A. M. Vibrational Studies of $(MLX_5)^{n-}$ Type Compounds. Dissertation, University of Canterbury, Christchurch, New Zealand, 1976.

(36) Allen, E. A.; Brisdon, B. J.; Edwards, D. A.; Fowles, G. W. A.; Williams, R. G. 890. Halide and Oxyhalide Complexes of Molybdenum and Tungsten. *J. Chem. Soc.* **1963**, 4649.

(37) Brown, D. 950. Some Oxychloro-Complexes of Quinquevalent Elements. *J. Chem. Soc.* **1964**, 4944.

(38) Srivastava, A. M.; Ackerman, J. F. Synthesis and Luminescence Properties of Cs_2NbOF_5 and Cs_2NbOCl_5 with Isolated $[NbOX_5]^{-2}$ (X = F$^-$, Cl$^-$) Octahedra. *Mater. Res. Bull.* **1991**, *26*, 443–448.

TOC Graphic

Supporting information for

Hybrid and Inorganic Vacancy-Ordered Double Perovskites A_2WCl$_6$

Emily E. Morgan,[1] Greggory T. Kent,[1] Arava Zohar, [1] Anthony O'Dea,[1] Guang Wu,[2]
Anthony K. Cheetham[*,1,3] and Ram Seshadri[*,1,2]

[1]Materials Department and Materials Research Laboratory, University of California, Santa Barbara, California 93106, United States

[2]Department of Chemistry and Biochemistry

University of California, Santa Barbara, California 93106, United States

[3]Department of Materials Science and Engineering

National University of Singapore, Singapore 117575, Singapore

E-mail: akc30@cam.ac.uk; seshadri@mrl.ucsb.edu

Table of contents

Section S1. Additional crystallographic details

Section S2. Additional photoluminescence details

Section S3. Additional details for Raman spectroscopy

Section S4. Additional XPS spectra

Section S1. Additional crystallographic details

Label	x	y	z	Occupancy	U_{eq}
W(1)	1/3	2/3	2/3	1	0.038
Cl(1)	0.17509	0.35020	0.60467	1	0.047
C(1)	2/3	1/3	0.54010	1	0.064
H(1A)	0.78024	0.30937	0.52550	1/6	0.096
H(1B)	0.69063	0.47087	0.52550	1/6	0.096
H(1C)	0.52913	0.21976	0.52550	1/6	0.096
N(1)	2/3	1/3	0.60630	1	0.051
H(1D)	0.78921	0.34308	0.61976	1/6	0.077
H(1E)	0.55387	0.21079	0.61976	1/6	0.077
H(1F)	0.65692	0.44613	0.61976	1/6	0.077

Table S1. Atomic coordinates and isotropic displacement parameters for MA_2WCl_6.

Label	x	y	z	Occupancy	U_{eq}
W(1)	0	0	0	1	0.024
Cs(1)	1/4	1/4	1/4	1	0.039
Cl(1)	−0.23026	0	0	1	0.037

Table S2. Atomic coordinates and isotropic displacement parameters for Cs_2WCl_6.

Label	x	y	z	Occupancy	U_{eq}
W(1)	0	0	0	1	0.025
Rb(1)	1/4	1/4	1/4	1	0.040
Cl(1)	-0.2374	0	0	1	0.042

Table S3. Atomic coordinates and isotropic displacement parameters for Rb_2WCl_6.

Label	x	y	z	Occupancy	U_{eq}
W(1)	1/2	1/2	1/2	1	0.051
Cs(1)	1/4	1/4	1/4	1	0.033
Cl(1)	0.2684	1/2	1/2	0.82	0.032
O(1)	0.314	1/2	1/2	0.18	0.032

Table S4. Atomic coordinates and isotropic displacement parameters for $Cs_2WO_{1.08}Cl_{4.92}$

	MA_2WCl_6	Cs_2WCl_6	Rb_2WCl_6	$Cs_2WO_{1.08}Cl_{4.92}$
CSD number	2250369	N/A	N/A	2250368
Empirical formula	$(CH_3NH_3)_2WCl_6$	Cs_2WCl_6	Rb_2WCl_6	$Cs_2WO_{1.08}Cl_{4.92}$
Formula weight (g/mol)	460.70	662.38	567.50	641.37
Temperature (K)	298	300	300	101
Crystal system	Trigonal	Cubic	Cubic	Cubic
Space group	R–3m	Fm–3m	Fm–3m	Fm–3m
Lattice parameters (Å)	$a=b=7.1125(14)$ $c=21.975(6)$	$a=b=c=$ 10.326451(55)	$a=b=c=$ 10.023918(349)	$a=b=c=10.23(2)$
Unit cell angles (°)	$\alpha=\beta=90$ $\gamma=120$	$\alpha=\beta=\gamma=90$	$\alpha=\beta=\gamma=90$	$\alpha=\beta=\gamma=90$
Volume (Å³)	962.7(4)	1101.167(17)	1007.193(105)	1072(6)
Z	3	4	4	4

Table S5. Unit cell details for MA_2WCl_6, Cs_2WCl_6, Rb_2WCl_6 and $Cs_2WO_{1.08}Cl_{4.92}$.

Formula	$(CH_3NH_3)_2WCl_6$	$Cs_2WO_{1.08}Cl_{4.92}$
Absorption coeff. (mm^{-1})	10.202	18.648
θ range for data collection (°)	2.78 to 24.712	3.448 to 30.370
Reflections collected	372	1803
Independent reflections	236	115
Completeness (%)	100	101.8
Refinement method	Full-matrix least-squares on F^2	Full-matrix least-squares on F^2
Data/restraints/parameters	236/0/17	115/0/8
Goodness-of-fit	1.014	1.133
Final R indices [I>2sigma(I)]	R=0.0233, wR=0.0478	R= 0.0254, wR= 0.0495
R indices (all data)	R=0.0258, wR=0.0482	R= 0.0300, wR= 0.0532
Largest diff. peak and hole	0.458 and -0.572	1.680 and -1.559

Table S6. Single-crystal XRD details for MA_2WCl_6 and $Cs_2WO_{1.08}Cl_{4.92}$.
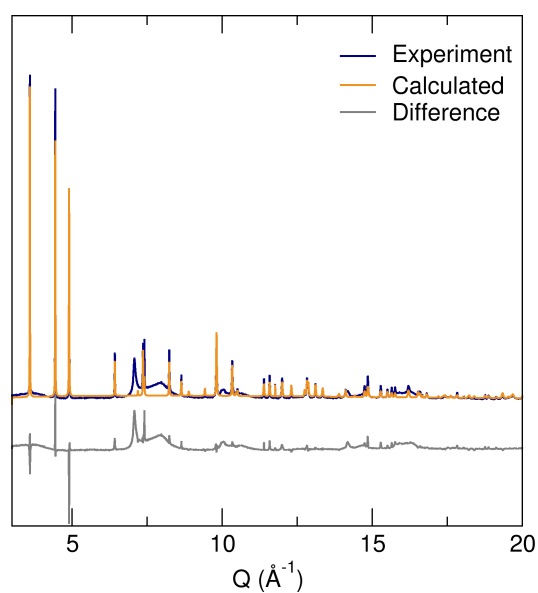
Figure S1. Rietveld refinement fit and difference of synchrotron X-ray diffraction data of MA_2WCl_6. Additional broad peaks in the diffraction pattern are due a small amount of epoxy used for sample sealing in the beam path.

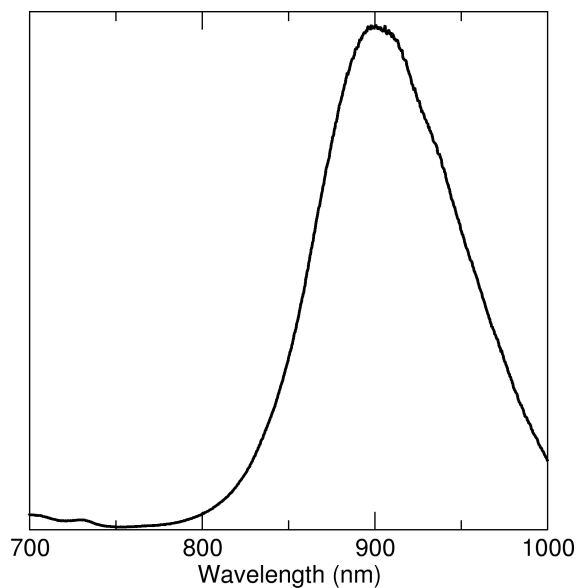**Section S2.** Additional luminescence spectrum

Figure S2. Photoluminescence spectra of $Cs_2WO_{1.08}Cl_{4.92}$ under 488 nm excitation.

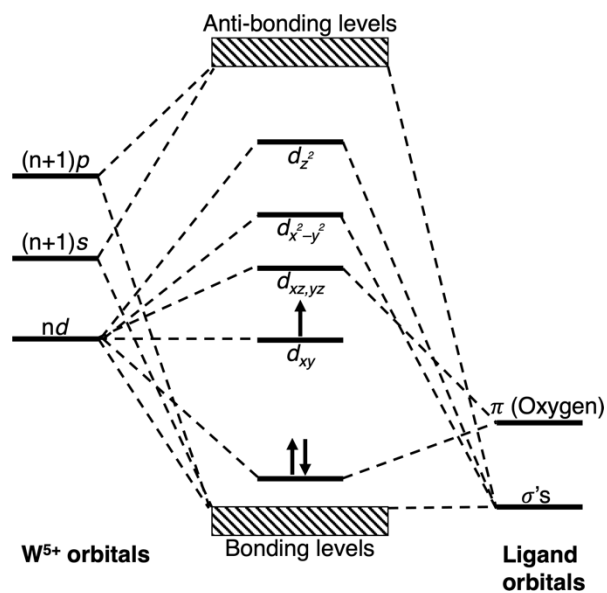**Figure S3.** Molecular orbital diagram for the $[WOCl_5]^{2-}$ ion. Recreated using the date provided in Gray, H. B.; Hare, C. R. *Inorg. Chem.* **1962**, 1, 363–368.

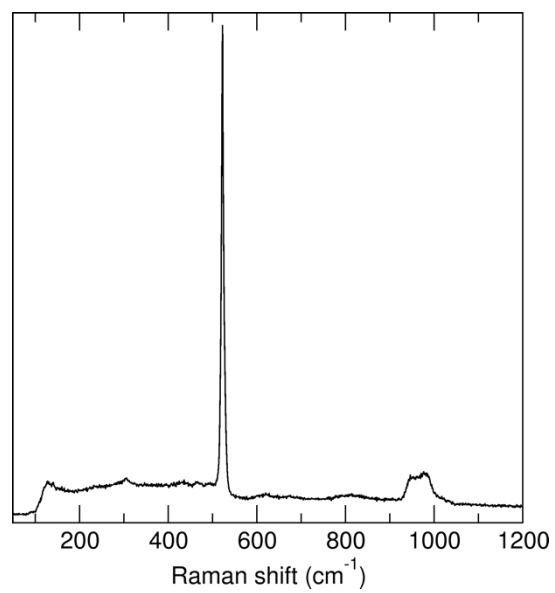**Section S3.** Additional details of Raman spectroscopy

Figure S4. Raman spectrum of monocrystalline silicon reference in the homemade air-free Raman cell. The glass window on the cell introduces some small peaks and baseline distortions to spectra.
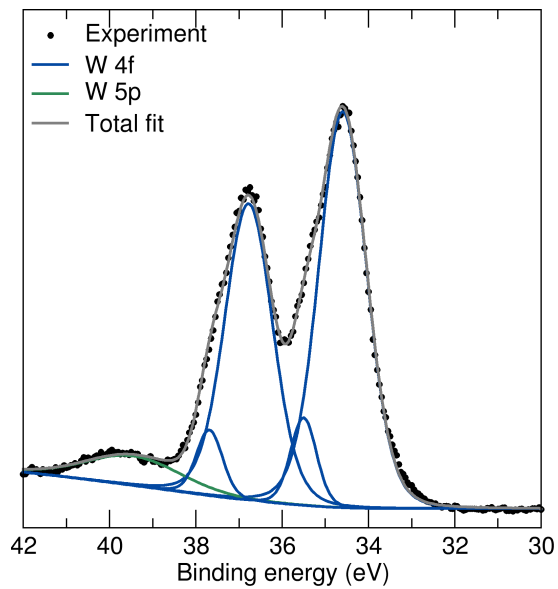
Section S4. Additional XPS spectra

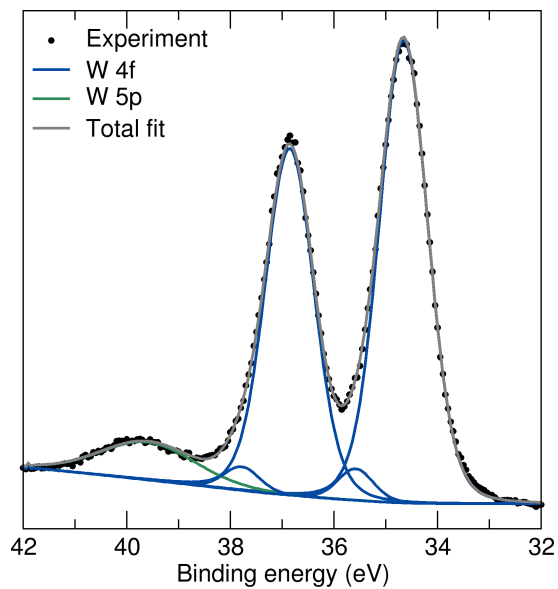**Figure S5**. Tungsten $4f$ high-resolution region of the XPS spectrum for MA_2WCl_6.

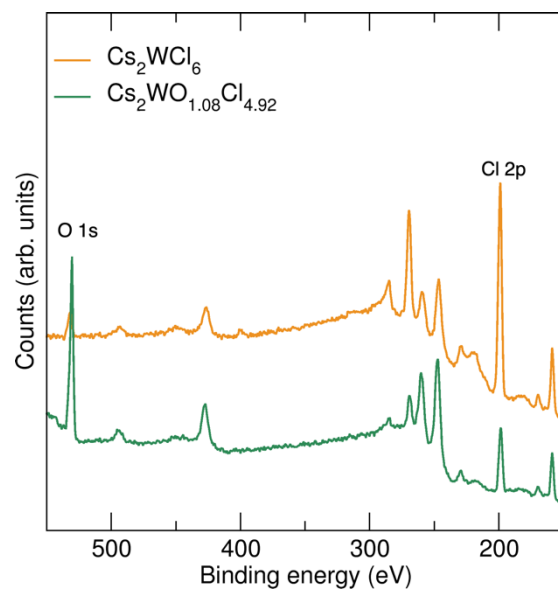**Figure S6**. Tungsten $4f$ high-resolution region of the XPS spectrum for Rb_2WCl_6.

Figure S7. XPS survey scans for Cs$_2$WCl$_6$ and Cs$_2$WO$_{1.08}$Cl$_{4.92}$ showing the O 1s and Cl 2p peaks.